



HAL
open science

Birth of a large volcanic edifice offshore Mayotte via lithosphere-scale dyke intrusion

Nathalie Feuillet, Stephan Jorry, Wayne C Crawford, Christine Deplus, Isabelle Thinon, Eric Jacques, Jean Marie Saurel, Anne Lemoine, Fabien Paquet, Claudio Satriano, et al.

► To cite this version:

Nathalie Feuillet, Stephan Jorry, Wayne C Crawford, Christine Deplus, Isabelle Thinon, et al.. Birth of a large volcanic edifice offshore Mayotte via lithosphere-scale dyke intrusion. *Nature Geoscience*, 2021, 14 (10), pp.787-795. 10.1038/s41561-021-00809-x . hal-03409680

HAL Id: hal-03409680

<https://hal.science/hal-03409680v1>

Submitted on 29 Oct 2021

HAL is a multi-disciplinary open access archive for the deposit and dissemination of scientific research documents, whether they are published or not. The documents may come from teaching and research institutions in France or abroad, or from public or private research centers.

L'archive ouverte pluridisciplinaire **HAL**, est destinée au dépôt et à la diffusion de documents scientifiques de niveau recherche, publiés ou non, émanant des établissements d'enseignement et de recherche français ou étrangers, des laboratoires publics ou privés.

1 **Birth of a large volcanic edifice offshore Mayotte via lithosphere-scale dike**
2 **intrusion**

3
4 Nathalie Feuillet^{1,*}, Stephan. Jorry², Wayne C. Crawford¹, Christine Deplus¹, Isabelle
5 Thinon³, Eric Jacques¹, Jean Marie Saurel¹, Anne Lemoine³, Fabien Paquet³, Claudio
6 Satriano¹, Chastity Aiken², Océane Foix¹, Philippe Kowalski¹, Angèle Laurent¹, Emmanuel
7 Rinnert², Cécile Cathalot², Jean-Pierre Donval², Vivien Guyader², Arnaud Gaillot², Carla
8 Scalabrin², Manuel Moreira¹, Aline Peltier¹, François Beauducel^{1,4}, Raphaël Grandin¹, Valérie
9 Ballu⁵, Romuald Daniel¹, Pascal Pelleau², Jérémy Gomez¹, Simon Besançon¹, Louis Geli²,
10 Pascal Bernard¹, Patrick Bachelery⁶, Yves Fouquet², Didier Bertil³, Arnaud Lemarchand¹,
11 Jérôme Van der Woerd⁷.

- 12
13 1. Université de Paris, Institut de physique du globe de Paris, CNRS, F-75005 Paris,
14 France
15 2. IFREMER, Unité Géosciences Marines, Technopole La Pointe du Diable, 29280
16 Plouzané, France
17 3. Bureau de Recherches Géologiques et Minières - BRGM, DGR/GBS, F-45060
18 Orléans, France
19 4. Université Grenoble Alpes, IRD, ISTERRE
20 5. Littoral ENVironnement et Sociétés (LIENSs) UMR7266, Université de La Rochelle -
21 CNRS, 2 rue Olympe de Gouges, 17000 La Rochelle
22 6. Université Clermont Auvergne, CNRS, IRD, OPGC, Laboratoire Magmas et Volcans,
23 F-63000 Clermont-Ferrand, France,
24 7. Institut de Physique du Globe de Strasbourg UMR7516 CNRS Université de
25 Strasbourg, 5 rue René Descartes 67000 Strasbourg, France
26
27
28

29 **Volcanic eruptions shape the Earth's surface and provide a window into deep Earth**
30 **processes. How the primary asthenospheric melts form, pond and ascend through the**
31 **lithosphere is, however, still poorly understood. Since 10 May 2018, magmatic activity**
32 **has occurred offshore eastern Mayotte (North Mozambique channel), associated with**
33 **large surface displacements, very low frequency earthquakes and exceptionally deep**
34 **earthquake swarms. Here we present geophysical and marine data from the MAYOBS1**
35 **cruise, which reveal that by May 2019, this activity formed a 820 m tall, ~5 km³ volcanic**
36 **edifice on the seafloor. This is the largest active submarine eruption ever documented.**
37 **Seismic and deformation data indicate that deep (> 55 km depth) magma reservoirs**
38 **were rapidly drained through dykes that intruded the entire lithosphere, and that pre-**
39 **existing subvertical faults in the mantle were reactivated beneath an ancient caldera**

40 **structure. We locate the new volcanic edifice at the tip of a 50 km-long ridge composed**
41 **of many other recent edifices and lava flows. This ridge is an extensional feature inside a**
42 **wide transtensional boundary that transfers strain between the East African and**
43 **Madagascar rifts. We propose that the massive eruption originated from hot**
44 **asthenosphere at the base of a thick old damaged lithosphere.**

45

46 Since May 10 2018, Mayotte Island (Comoros archipelago, Indian Ocean, *Figure 1a*) has
47 experienced a major magmatic event off its eastern coast. This event generated more than
48 11000 detectable earthquakes (up to Mw 5.9), surface deformation rates of up to 200 mm/year
49 and unusual very low frequency (VLF) earthquakes ^{1,2,3}. As of May 2021 (the time of writing),
50 Mayotte is still deforming and both VLF events and earthquakes with Mw up to 4 are still
51 being recorded.

52 Prior to this event, no recent eruption or significant seismic activity was reported around
53 Mayotte ². Only two earthquakes were detected within 100 km of the island since 1972 ⁴ and
54 the most recent volcanic exposure is a 4-6 kyr-old pumice layer sampled in the lagoon
55 surrounding the island ⁵.

56 Recent geodynamic reconstructions suggest that the Comoros archipelago was built on ~150
57 Ma old oceanic lithosphere accreted to accommodate the opening of the Western Somali
58 Basin ⁶. The Comorian volcanism may result from partial melting of the base of this old
59 lithosphere in interaction with plume material ^{7,8,9}, possibly super plumes originating from
60 Africa ^{10,11,12}, and may have been controlled by lithospheric deformation ^{13 14}. Subaerial
61 volcanic activity on Mayotte island began 11 My ago ¹³. Well-preserved cones, tuff rings and
62 maar craters in the Northeastern part of the island (on Petite Terre and in and around
63 Mamoudzou ^{15,7} and further offshore ¹⁶ (*Figure 1b*) testify to relatively recent (probably

64 Holocene, ⁷) subaerial explosive volcanic activity. Gas emissions on Petite-Terre indicate
65 magma degassing ¹⁷.

66

67 **The discovery of the eruption and the new volcanic edifice**

68 To determine the origin of the seismicity and deformation and to search for any seafloor
69 volcanic activity, we deployed Ocean Bottom Seismometers (OBS) with attached Absolute
70 Pressure Gauges (APG) and acquired high-resolution marine data (bathymetry, seafloor and
71 water column backscatter), rock dredges and CTD (Conductivity-Temperature-Depth)-
72 Rosette during the MAYOBS1 (2-19 May 2019) cruise aboard the R/V Marion Dufresne ¹⁸.

73 A systematic 12 kHz multibeam echosounder survey east of Mayotte, revealed a 820 m tall
74 new volcanic edifice (NVE) 50 km east of Mayotte (*Figure 1*). The NVE was detected by
75 comparing our data to those acquired during a 2014 survey by the French Naval Hydrographic
76 and Oceanographic Service (SHOM) ¹⁹ (*Figure 2a*). The edifice sits on an area that, in the
77 2014 seafloor topography, was locally almost flat at around 3300 m below sea level (bsl).

78 The NVE has grown on the lower insular slope of Mayotte, at the eastern tip of a WNW-ESE
79 trending volcanic ridge (Mayotte ridge) on the submarine flank of Mayotte (*Figure 1*). The
80 NVE and many other volcanic features along the ridge have high acoustic reflectivity
81 compared to the surrounding sediments, indicating recent volcanic activity all along the ridge
82 (*Figure 1c and extended data Figures 1,2,3*). The ridge is 50 km long, extending from the
83 most recent subaerial cones and maar craters on Grande-Terre and Petite-Terre islands (MPT
84 Volcanic zone) to the NVE (*Figure 1b*). It is divided into two main segments, one on the
85 upper slope (western) and one on the mid- to lower-slope (eastern). The eastern segment
86 trends N130°E and is made of many constructional features similar to mafic submarine
87 eruption features observed elsewhere ^{20,21,22}: cones up to 2 km-wide and 500 m-high, probably
88 monogenetic; lava flows with smooth bathymetry, elongated ridges with steep slopes and

89 varying orientations, which could result from dykes in more sedimented areas (*Figure 1 and*
90 *extended data Figure 2d,e*).

91 The western segment is made of volcanic features having more complex morphologies and
92 emplaced along different directions (*Figure 1b and extended data Figure 2b,c*). The main
93 features are: i) Two N40°E and N120°E trending sets of high-backscatter cones and lava
94 flows, northeast and southeast of Petite-Terre, respectively. These sets converge toward the
95 onshore maar craters of Petite-Terre and may have been emplaced along pre-existing fractures
96 or faults; ii) a horse-shoe shaped edifice (the Horseshoe) with a 3.5 km wide cone, steep
97 slopes and a large collapse-induced scar. East of the Horseshoe, several smaller cones and
98 volcanic features are aligned E-W, suggesting eruptive fissures. Large lava flows originate
99 from this fissure system. iii) a 4 km-wide circular structure (the Crown), whose rim is
100 crowned by seven 1 km-wide, 100-150m high volcanic cones. Their arrangement suggests
101 typical post-caldera domes²³. West of the Crown, submarine canyons and slope failure scars
102 terminate at a N-S trending slope break that may be controlled by faulting. The Crown
103 appears to sit inside a larger 10 km wide flat depression, bounded by faults and fissures,
104 which could be the remnant of an ancient caldera collapse.

105 The NVE is located at the eastern tip of the eastern segment of the Mayotte ridge (*Figures*
106 *1b*). In May 2019, its summit rose to 2580 m bsl. Its central peak resembles a pyramid with
107 steep and smooth slopes (*Figure 2a and extended data Figure 3*). Radial ridges, up to 300 m
108 thick and extending up to 5 km from the central pyramid, display hummocky morphology
109 similar to that observed along mid-ocean volcanic ridges²⁴ and active seamounts²² and
110 probably correspond to coalesced pillow lava mounds²¹. Beyond and in-between the
111 hummocky ridges, flat areas up to 100 m thick, with high backscatter, could indicate
112 channelized lava flows or sheet flows emplaced at high effusion rates²⁵. We calculate the
113 volume of material corresponding to the 2014- 2019 seafloor depth difference to be at least

114 $5.0 \pm 0.3 \text{ km}^3$ (*Figure 2b*). Popping fragments of very fresh basanitic pillow lavas (SiO₂ 47
115 wt%, Na₂O + K₂O 7.1 wt%, MgO 5.7 wt% ²⁶) were dredged on the northeastern flank of the
116 NVE, near its summit (see *Figure 2a* for sample location and *supplementary S1*). The lavas,
117 similar to other basanites sampled in northern Mayotte ⁷ are aphyric with rare
118 microphenocrysts of olivine (Fo70) and Ti-magnetite.

119 A ~1900-m high, vertical acoustic plume, rising through the water column from the NVE
120 summit to ~800 m below the sea surface, was imaged several times during the cruise using
121 the ship-borne multibeam echosounder (*Figure 3*, supplementary movie 1). A vertical
122 CTD/rosette cast to 3137m depth above the northern flank of the NVE, 1000m offset from the
123 summit, showed strong geochemical signatures. High volatile concentrations (H₂ = 550nM,
124 CH₄ = 831 nM, CO₂ = 34 μM), high turbidity and high total alkalinity values were associated
125 with temperature and pH anomalies (respectively 0.2°C and 1 pH unit) ²⁷ and *Extended data*
126 *Fig. 4*). Such chemical anomalies are characteristic of submarine eruptions and may reflect
127 magma degassing ²⁸, molten lava interaction with seawater ²⁹ or fluid/water discharge from
128 subsurface storage zones in the crust or sedimentary cover ³⁰. The height and the strong
129 backscatter signature of the acoustic plume suggest that a mixture of solid particles
130 (pyroclastic/hyaloclastic jet ²⁸) and/or differentiated fluid phases (droplets, hydrate-coated
131 bubbles or free gas ³¹) are driven upward through the water column from the NVE summit ³².
132 High turbidity measured at water depths below 2500 m, on the northern flank of the NVE,
133 likely indicates the presence of these particles ³³. Both the multiple observations of the vertical
134 acoustic plume at the summit of the NVE and the high H₂ concentration 1 km away indicate
135 that the eruption was likely on-going in May 2019 ²⁹.

136 In the upper slope zone, 30 km away from the volcano, two, ~1000-m high acoustic plumes
137 were detected above the Horseshoe edifice (*Figure 1 and extended data Figure 5, movie 2*)
138 but no significant changes in seafloor morphology or reflectivity were detected.

139

140 **The seismicity and VLF events relocated by OBS data**

141 The combined land-OBS network of seismic stations (supplementary Figure S2.1) detected
142 17000 events between February 25 and May 6, 2019. We manually relocated about 800 of the
143 largest earthquakes onboard (*see method and supplementary S2*). Ninety-four percent of the
144 earthquakes cluster beneath the western segment of the Mayotte ridge, 40 km west of the
145 NVE and 5 to 15 km east of Petite-Terre (swarm 1, *Figure 1*). Almost all of the remaining
146 events form a secondary swarm beneath the northwestern tip of the eastern segment, 30 km
147 from Petite-Terre and 20 km from the NVE (swarm 2, *Figure 1*). A few events are also
148 scattered along the eastern segment. We searched the full OBS-land catalog for events
149 beneath the NVE, but found none. The located earthquakes are all very deep, ranging from
150 25 ± 5 to 50 ± 5 km. In addition, all P-S arrival delays recorded by an OBS deployed for 48h
151 above the main swarm were greater than 3 seconds, indicating no events less than 20 km
152 depth (*Figure 4, extended data Figure 6b, method and supplementary S2.2*). The land-OBS
153 catalog does not show any evidence for seismicity migration, but it only represents a two-
154 month “snapshot” of the activity. To extend the observational time window, we relocated 139
155 earthquakes recorded by the land stations between May 2018 and the first OBS deployment.
156 All the events were beneath the volcanic ridge (*extended data fig. 6a*). During the first weeks
157 of the crisis, they were mainly located beneath the northwestern tip of the eastern segment,
158 between 30 and 50 km depth, whereas in the last two weeks of June, a few events occurred
159 closer to the NVE and between 30km-depth and the surface.

160 In addition to the high frequency seismicity, VLF events were recorded by the OBSs
161 wideband hydrophones. Their waveforms are similar to those of the globally detected
162 November 11 2018 event (exponentially decaying monochromatic signals of approximately
163 2000s duration, with dominant period of ~ 15 s and polarized Rayleigh waves), suggesting

164 repeated excitation of the same radiating source. We located 84 VLF events using waveform
165 cross-correlation (*see method and supplementary S2.3*), all of them are most probably above
166 seismic swarm 1 (*Figures 4 and extended data Figure 6b*), at a mean depth of 22 ± 15 km.

167

168 **GNSS data and APG modeling**

169 The GNSS network includes nine stations on Mayotte Island and two far field stations at
170 Diego Suarez and Grande Glorieuse islands. The geometry is not optimal, preventing geodetic
171 inversions for complicated structures or media. We performed Bayesian inversions³⁴ of the
172 data using a point source in an elastic half-space with two distinct analytical formalisms: an
173 isotropic point source³⁵ and a point compound dislocation model (pCDM,³⁶ *see method,*
174 *supplementary S3 and extended data Figure 7*). In both cases, the results indicate ~ 5 km³
175 deflation of a deep reservoir (> 30 km). The simplest and most robust model is the deflation
176 of ~ 40 km deep isotropic source below the eastern segment of the Mayotte ridge. An increase
177 in absolute seafloor pressure measured by all APGs on the OBS frames, interpreted as
178 seafloor subsidence, is compatible with these models (*see method, supplementary S3,*
179 *extended data Figure 7d*).

180

181 **Magma reservoirs and chronology of the eruption**

182 Most of our located seismicity and modelled GNSS sources lie in the lithospheric mantle,
183 beneath the ~ 17 km deep Moho³⁷. Volcanic seismicity this deep is rarely documented^{38,39},
184 especially in dense swarms during eruptions.

185 The distribution of the seismicity in the first weeks of the crisis suggests a dyke migration
186 from the mid-slope zone to the NVE, along the eastern segment of the Mayotte ridge. This is
187 also supported by the migration of the largest earthquakes' Centroid Moment Tensor depths⁴⁰
188 towards the surface (*extended data Figures 6c and 8*) and agrees well with^{1,2}. The
189 earthquakes show strike-slip focal mechanisms compatible with a least compressive principal

190 stress orthogonal to the eastern segment of the ridge. Similar stress trends have been observed
191 during dyking events beneath the Izu peninsula in Japan ⁴¹ and in Iceland ⁴² but at much
192 shallower depths, where they were interpreted as seismic shear faulting caused by stress
193 transfer to the surrounding vertical faults in response to dyke opening and propagation.

194 During the first six weeks of the crisis, the magma migrated 20 km laterally along the eastern
195 segment of the Mayotte ridge, then upward (*Figure 4 and extended data Figure 8*). The
196 building of the NVE may have begun in July 2018, once the dyke reached close to the surface
197 ^{2,1} allowing for high magma flow rates and rapid ensuing growth. On the basis of this
198 assumption, we estimate a minimum mean lava flow rate of $\sim 180\text{m}^3\text{s}^{-1}$ between the start of
199 the eruption on the seafloor and our survey (~ 11 months). The local stress probably
200 decreased considerably once the magma path to the NVE was opened, as is observed during
201 many eruptions involving dyke propagation ⁴³, which would explain why no earthquakes were
202 detected beneath the NVE during the OBS deployment.

203 After the dike reached the near surface, seismicity resumed beneath the mid- and upper-slope
204 volcanic zones (*Figure 4 and extended data Figures 6a,b and 8*) and its pattern appears to be
205 constant since September 2018 ². This stationary seismicity could be caused by stress
206 perturbation along pre-existing structures and/or fluid (gas, magma or water) motions. The
207 swarm 1 earthquakes cluster beneath the ancient caldera structure inferred from our high-
208 resolution bathymetry (*Figure 1c and extended data Figure 6b and 8*). This seismicity could
209 indicate activation of pre-existing subvertical faults ⁴⁴ above a deep (> 55 km) depleting
210 reservoir (R1,4), as has been observed during caldera collapse events ⁴⁵: if so, these faults
211 would be much deeper than documented elsewhere. Analog models for collapse of a caldera
212 with a high-roof aspect ratio (thickness/width $\gg 1$) indicate reverse fault motions during an
213 initial downsag stage ⁴⁶, in agreement with the focal mechanism of the May 14, 2019 Mw4.9
214 swarm 1 region earthquake (*Figure 4 and extended data Figure 8*) and ¹.

215 The VLF events located above swarm 1 may be generated by the resonance of a fluid-filled
216 (magma, gas or hydrothermal) shallower cavity or a fluid-filled crack, most probably at the
217 base of the crust. The characteristic frequency and duration of these events are very different
218 from VLF events typically observed in volcanic zones e.g. ⁴⁷. Simple up-scaling of fluid
219 resonance models ^{48,49} implies a shallower reservoir size of several kilometres (R3, *Figure 4*).
220 The excitation mechanism could be rapid slip and related strain on faults close to the
221 reservoir, or episodic collapse of a piston at the base of this shallow reservoir ⁴⁷. The acoustic
222 plumes emanating from the overlying Horseshoe edifice may result from actively degassing
223 of this shallower reservoir.

224 Both the distribution of seismicity over time and the surface deformation models suggest the
225 drainage of an exceptionally deep reservoir by a dyke that propagated from the base of the
226 brittle lithosphere to the eastern portion of the Mayotte ridge, possibly intersecting another
227 vertical storage zone below seismic swarm 2 before reaching the surface (*R2, Figure 4 and*
228 *extended data Figure 8*). Within the uncertainties the GNSS isotropic model may reflect the
229 drainage of reservoir R2 in the brittle lithosphere. The deeper reservoir (R1) may have slowly
230 recharged from the asthenosphere before reaching tensile failure in May 2018 ⁵⁰.

231 **Magma roots and paths.**

232 The eastern segment of the Mayotte ridge, along which the dike propagated, has the same
233 orientation as many other volcanic features over a range of scales (Quaternary dykes, volcanic
234 vent alignments, ridges and volcanic rift zones) in the northeastern part of Mayotte Island ¹⁵
235 and in and around the other Comoros islands ^{13,51} (*Figure 5 and extended data Figure 9*). The
236 left-lateral en-echelon arrangement of these features resembles that of extensional tectonic
237 structures in a context of oblique extension (i.e in segmented and diffuse strike-slip fault
238 systems ⁵² or highly-oblique rifting (e.g. ^{53,54,55}). We infer that the Mayotte ridge results from
239 the interplay between volcanism and tectonics. The location and orientation of the volcanic

240 features may be in part controlled by the pre-existing Mesozoic fracture zones ⁶ but they
241 probably also emplace along new tectonic structures. These tectonic structures are extensional
242 (fissures or step-overs) and open as a result of volcano-tectonic interactions in a wide E-W
243 striking zone, to transfer the strain between the N-S striking offshore branches of the East
244 African rift ⁵⁶ and the grabens of Madagascar (Aloatra and Ankai) ⁵⁷. In this context, high
245 strain rates ⁵⁴ or highly damaged zones may develop ⁵⁸ (*Figure 5a inset*) in between the main
246 en-echelon extensional structures. Such zones may constitute high-permeability zones where
247 large magmatic reservoirs can develop. The main Comoros volcanic islands may have grown
248 above such zones.

249 Between Mayotte and Madagascar, the lithosphere-asthenosphere boundary (LAB) is a sharp
250 limit between a high-velocity 150 Ma lithosphere and a low-velocity asthenosphere, at about
251 70 km depth ^{59,60}. The low-velocity asthenosphere is interpreted as hot material spreading
252 beneath the Mascarene basin and beyond ⁶¹. Heating of the base of the oceanic
253 lithosphere damaged by extensional tectonic and loaded by Mayotte island ⁶² may favour the
254 ponding of large volumes of buoyant melts. Pore pressure increase in these zones may in turn
255 favour failure of deep reservoirs and faults inside the brittle lithosphere

256 **The largest eruption ever documented in submarine domain**

257 The NVE extruded volume (as of May 2019) is 30 to 1000 times larger than that estimated for
258 other deep-sea eruptions ^{63,25,64,21}. It is difficult to evaluate the dense rock equivalent (DRE)
259 volume ²⁰, but, taking an upper bound of 50% for the DRE factor ⁶⁵, compatible with the 40%
260 vesicularity of our rock sample ²⁶, the DRE erupted volume could be as large as 2.5 km³,
261 which is larger than the 1.2 to 1.5 km³ Havre silicic eruption ⁶⁶), previously considered to be
262 the largest documented submarine eruption. It would be 2.5 times larger than the Bardabunga
263 eruption (Iceland's largest eruption of the last two centuries) ⁴³ and only 6 times less than
264 Iceland's 1783-1784 Laki eruption, considered to be one of the largest basaltic eruptions

265 witnessed by humanity⁶⁷. The volumes and flux of emitted lava during the Mayotte magmatic
266 event are comparable to those observed during eruptions at Earth's largest hot spots (Hawaii,
267 Iceland,^{43,68} and one quarter of that emplaced yearly over the entire mid-ocean ridge
268 system (mean estimate from spreading rates over the last 80 Ma⁶⁹). It thus represents a
269 considerable input in terms of CO₂ flux⁷⁰.

270 Future scenarios could include a new caldera collapse, submarine eruptions on the upper
271 slope, or onshore eruptions. Large lava flows and cones on the upper slope and onshore
272 Mayotte indicate that this has occurred in the past. Since the discovery of the NVE, an
273 observatory has been established to monitor activity in real time (REVOSIMA⁷¹) and return
274 cruises continue to follow the evolution of the eruption and edifices.

275 **References**

- 276 1 Cesca, S. *et al.* Drainage of a deep magma reservoir near Mayotte inferred from
277 seismicity and deformation. *Nat. Geosci.* **13**, 87-93, doi:10.1038/s41561-019-0505-5
278 (2020).
- 279 2 Lemoine, A., Bertil, D., Roullé, A. & Briole, P. The volcano-tectonic crisis of 2018
280 east of Mayotte, Comoros islands. *Geophys. J. Int.*
- 281 3 REVOSIMA, R. d. s. V. e. S. d. M. REVOSIMA (2020), Bulletin n°18 de l'activité
282 sismo-volcanique à Mayotte, du 1 au 31 août, . Report No. 2680-1205, (2020).
- 283 4 U.S. Geological Survey. (<https://earthquake.usgs.gov/earthquakes/search> 2019).
- 284 5 Zinke, J., Reijmer, J. & Thomassin, B. Systems tracts sedimentology in the lagoon of
285 Mayotte associated with the Holocene transgression. *Sedimentary Geology* **160**, 57-79
286 (2003).
- 287 6 Phethean, J. J. *et al.* Madagascar's escape from Africa: A high-resolution plate
288 reconstruction for the Western Somalian Basin and implications for supercontinent
289 dispersal. *Geochemistry, Geophysics, Geosystems* **17**, 5036-5055 (2016).
- 290 7 Pelleter, A.-A. *et al.* Melilite-bearing lavas in Mayotte (France): An insight into the
291 mantle source below the Comores. *Lithos* **208-209**, 281-297,
292 doi:10.1016/j.lithos.2014.09.012 (2014).
- 293 8 Class, C., Goldstein, S. L., Altherr, R. & Bachelery, P. The process of plume-
294 lithosphere interactions in the ocean basins—the case of Grande Comore. *Journal of*
295 *Petrology* **39**, 881-903 (1998).
- 296 9 Claude-Ivanaj, C., Bourdon, B. & Allègre, C. J. Ra–Th–Sr isotope systematics in
297 Grande Comore Island: a case study of plume–lithosphere interaction. *Earth and*
298 *Planetary Science Letters* **164**, 99-117 (1998).
- 299 10 Ebinger, C. J. & Sleep, N. Cenozoic magmatism throughout east Africa resulting from
300 impact of a single plume. *Nature* **395**, 788-791 (1998).

- 301 11 Reiss, M., Long, M. & Creasy, N. Lowermost mantle anisotropy beneath Africa from
302 differential SKS-SKKS shear-wave splitting. *Journal of Geophysical Research: Solid*
303 *Earth* **124**, 8540-8564 (2019).
- 304 12 Class, C., Goldstein, S. L., Stute, M., Kurz, M. D. & Schlosser, P. Grand Comore
305 Island: A well-constrained “low $^3\text{He}/^4\text{He}$ ” mantle plume. *Earth and Planetary*
306 *Science Letters* **233**, 391-409 (2005).
- 307 13 Nougier, J., Cantagrel, J. & Karche, J. The Comores archipelago in the western Indian
308 Ocean: volcanology, geochronology and geodynamic setting. *J. Afr. Earth Sci. (1983)*
309 **5**, 135-145 (1986).
- 310 14 Michon, L. in *Active volcanoes of the southwest Indian Ocean* (eds P Bachelery, J-F
311 Lénat, A Di Muro, & L Michon) 233-244 (Springer, 2016).
- 312 15 Nehlig, P. *et al.* Report French geological map (1/30 000), sheet Mayotte (1179).
313 Orléans: BRGM, 74 p. . **Geological map by Lacquement F., Nehlig P, Bernard J.**
314 **(2013).** (2013).
- 315 16 Audru, J.-C., Guennoc, P., Thinon, I. & Abellard, O. Bathymay : la structure sous-
316 marine de Mayotte révélée par l'imagerie multifaisceaux. *Comptes Rendus Geoscience*
317 **338**, 1240-1249, doi:10.1016/j.crte.2006.07.010 (2006).
- 318 17 Sanjuan, B. *et al.* Estimation du potentiel géothermique de Mayotte : Phase 2 - Étape
319 2. Investigations géologiques, géochimiques et géophysiques complémentaires,
320 synthèse des résultats. 82 (BRGM, Orléans, France, 2008).
- 321 18 Feuillet, N. MAYOBS1 French Oceanographic cruise, RV Marion Dufresne.
322 doi:https://doi.org/10.17600/18001217 (2019).
- 323 19 SHOM. (2014).
- 324 20 Rubin, K. H. *et al.* Volcanic eruptions in the deep sea. *Oceanography* **25**, 142-157
325 (2012).
- 326 21 Chadwick Jr, W. W. *et al.* Recent eruptions between 2012-2018 discovered at West
327 Mata submarine volcano (NE Lau Basin, SW Pacific) and characterized by new ship,
328 AUV, and ROV data. *Frontiers in Marine Science* **6**, 495 (2019).
- 329 22 Clague, D. A. *et al.* Structure of Lō'ihi Seamount, Hawai'i, and Lava Flow
330 Morphology from High-resolution Mapping. *Frontiers in Earth Science* **7**, 58 (2019).
- 331 23 Cole, J., Milner, D. & Spinks, K. Calderas and caldera structures: a review. *Earth-*
332 *Science Reviews* **69**, 1-26 (2005).
- 333 24 Yeo, I. A. & Searle, R. High-resolution Remotely Operated Vehicle (ROV) mapping
334 of a slow-spreading ridge: Mid-Atlantic Ridge 45° N. *Geochemistry, Geophysics,*
335 *Geosystems* **14**, 1693-1702 (2013).
- 336 25 Clague, D. A. *et al.* High-resolution AUV mapping and targeted ROV observations of
337 three historical lava flows at Axial Seamount. *Oceanography* **30**, 82-99 (2017).
- 338 26 Bachelery, P. *et al.* Petrological and Geochemical Characterization of the Lava from
339 the 2018-2019 Mayotte Eruption: First Results. *AGUFM* **2019**, V52D-06 (2019).
- 340 27 Cathalot, C. *et al.* Acoustic and Geochemical Anomalies in the Water Column around
341 the Newly Formed Volcano offshore Mayotte Island. *AGUFM* **2019**, V52D-05 (2019).
- 342 28 Resing, J. A. *et al.* Active submarine eruption of boninite in the northeastern Lau
343 Basin. *Nature Geoscience* **4**, 799-806 (2011).
- 344 29 Baumberger, T. *et al.* Understanding a submarine eruption through time series
345 hydrothermal plume sampling of dissolved and particulate constituents: W est M ata,
346 2008–2012. *Geochemistry, Geophysics, Geosystems* **15**, 4631-4650 (2014).
- 347 30 Baker, E. T. *et al.* Hydrothermal discharge during submarine eruptions: The
348 importance of detection, response, and new technology. *Oceanography* **25**, 128-141
349 (2012).

- 350 31 Chadwick, W. W. *et al.* Imaging of CO₂ bubble plumes above an erupting submarine
351 volcano, NW Rota-1, Mariana Arc. *Geochemistry, Geophysics, Geosystems* **15**, 4325-
352 4342 (2014).
- 353 32 Somoza, L. *et al.* Evolution of submarine eruptive activity during the 2011–2012 E I H
354 ierro event as documented by hydroacoustic images and remotely operated vehicle
355 observations. *Geochemistry, Geophysics, Geosystems* **18**, 3109-3137 (2017).
- 356 33 Sohn, R. A. *et al.* Explosive volcanism on the ultraslow-spreading Gakkel ridge,
357 Arctic Ocean. *Nature* **453**, 1236-1238 (2008).
- 358 34 Tarantola, A. Linearized inversion of seismic reflection data. *Geophysical prospecting*
359 **32**, 998-1015 (1984).
- 360 35 Anderson, E. Dynamics of formation of cone-sheets, ring-dikes, and cauldron
361 subsidences: Royal Society of Edinburgh Proceedings, v. 56. (1936).
- 362 36 Nikkhoo, M., Walter, T. R., Lundgren, P. R. & Prats-Iraola, P. Compound dislocation
363 models (CDMs) for volcano deformation analyses. *Geophysical Journal International*,
364 ggw427 (2016).
- 365 37 Dofal, A., Fontaine, F. R., Michon, L., Barruol, G. & Tkalčić, H. in *AGU Fall Meeting*
366 *2018*. (AGU).
- 367 38 Merz, D., Caplan-Auerbach, J. & Thurber, C. Seismicity and Velocity Structure of
368 Lō'ihi Submarine Volcano and Southeastern Hawai'i. *Journal of Geophysical*
369 *Research: Solid Earth* **124**, 11380-11393 (2019).
- 370 39 Wolfe, C., Okubo, P. & Shearer, P. Mantle fault zone beneath Kilauea Volcano,
371 Hawaii. *Science* **300**, 478-480, doi:10.1126/science.1082205 (2003).
- 372 40 Ekström, G., Nettles, M. & Dziewoński, A. The global CMT project 2004–2010:
373 Centroid-moment tensors for 13,017 earthquakes. *Physics of the Earth and Planetary*
374 *Interiors* **200**, 1-9 (2012).
- 375 41 Toda, S., Stein, R. & Sagiya, T. Evidence from the AD 2000 Izu islands earthquake
376 swarm that stressing rate governs seismicity. *Nature* **419**, 58-61,
377 doi:10.1038/nature00997 (2002).
- 378 42 Ágústsdóttir, T. *et al.* Strike-slip faulting during the 2014 Bárðarbunga-Holuhraun
379 dike intrusion, central Iceland. *Geophysical Research Letters* **43**, 1495-1503 (2016).
- 380 43 Sigmundsson, F. *et al.* Segmented lateral dyke growth in a rifting event at
381 Bárðarbunga volcanic system, Iceland. *Nature* **517**, 191-195, doi:10.1038/nature14111
382 (2015).
- 383 44 Jacques, E. *et al.* in *AGU* (Online everywhere, 2020).
- 384 45 Gudmundsson, M. T. *et al.* Gradual caldera collapse at Bárðarbunga volcano, Iceland,
385 regulated by lateral magma outflow. *Science* **353**, aaf8988 (2016).
- 386 46 Roche, O., Druitt, T. & Merle, O. Experimental study of caldera formation. *Journal of*
387 *Geophysical Research: Solid Earth* **105**, 395-416 (2000).
- 388 47 Kumagai, H. *et al.* Very-Long-Period Seismic Signals and Caldera Formation at
389 Miyake Island, Japan. *Science* **293**, 687-690, doi:10.1126/science.1062136 (2001).
- 390 48 Fazio, M., Alparone, S., Benson, P. M., Cannata, A. & Vinciguerra, S. Genesis and
391 mechanisms controlling tornillo seismo-volcanic events in volcanic areas. *Scientific*
392 *reports* **9**, 1-11 (2019).
- 393 49 Maeda, Y. & Kumagai, H. A generalized equation for the resonance frequencies of a
394 fluid-filled crack. *Geophysical Journal International* **209**, 192-201 (2017).
- 395 50 Sigmundsson, F. *et al.* Unexpected large eruptions from buoyant magma bodies within
396 viscoelastic crust. *Nature Communications* **11**, 1-11 (2020).

- 397 51 Famin, V., Michon, L. & Bourhane, A. The Comoros archipelago: a right-lateral
398 transform boundary between the Somalia and Lwandle plates. *Tectonophysics* **789**,
399 228539 (2020).
- 400 52 Armijo, R., Meyer, B., Navarro, S., King, G. & Barka, A. Asymmetric slip
401 partitioning in the Sea of Marmara pull-apart: A clue to propagation processes of the
402 North Anatolian fault? *Terra Nova* **14**, 80-86 (2002).
- 403 53 Dauteuil, O. & Brun, J.-P. Oblique rifting in a slow-spreading ridge. *Nature* **361**, 145-
404 148 (1993).
- 405 54 Brune, S. Evolution of stress and fault patterns in oblique rift systems: 3-D numerical
406 lithospheric - scale experiments from rift to breakup. *Geochemistry, Geophysics,*
407 *Geosystems* **15**, 3392-3415 (2014).
- 408 55 Pagli, C., Yun, S.-H., Ebinger, C., Keir, D. & Wang, H. Strike-slip tectonics during
409 rift linkage. *Geology* **47**, 31-34 (2019).
- 410 56 Franke, D. *et al.* The offshore East African Rift System: Structural framework at the
411 toe of a juvenile rift. *Tectonics* **34**, 2086-2104 (2015).
- 412 57 Rufer, D., Preusser, F., Schreurs, G., Gnos, E. & Berger, A. Late Quaternary history of
413 the Vakinankaratra volcanic field (central Madagascar): insights from luminescence
414 dating of phreatomagmatic eruption deposits. *Bulletin of volcanology* **76**, 817 (2014).
- 415 58 Peacock, D. & Anderson, M. THE SCALING OF PULL - APARTS AND
416 IMPLICATIONS FOR FLUID FLOW IN AREAS WITH STRIKE-SLIP FAULTS.
417 *Journal of Petroleum Geology* **35**, 389-399 (2012).
- 418 59 Pratt, M. J. *et al.* Shear velocity structure of the crust and upper mantle of Madagascar
419 derived from surface wave tomography. *Earth and Planetary Science Letters* **458**,
420 405-417 (2017).
- 421 60 Mazzullo, A. *et al.* Anisotropic Tomography Around La Réunion Island From
422 Rayleigh Waves. *J. Geophys. Res. Solid Earth* **122**, 9132-9148,
423 doi:10.1002/2017JB014354 (2017).
- 424 61 Barruol, G. *et al.* Large-scale flow of Indian Ocean asthenosphere driven by Réunion
425 plume. *Nat. Geosci.* **12**, 1043-1049, doi:10.1038/s41561-019-0479-3 (2019).
- 426 62 Zhong, S. & Watts, A. Lithospheric deformation induced by loading of the Hawaiian
427 Islands and its implications for mantle rheology. *Journal of Geophysical Research:*
428 *Solid Earth* **118**, 6025-6048 (2013).
- 429 63 Watts, A. B. *et al.* Rapid rates of growth and collapse of Monowai submarine volcano
430 in the Kermadec Arc. *Nature Geosci* **5**, 510-515, doi:10.1038/ngeo1473 (2012).
- 431 64 Chadwick Jr, W. W. *et al.* A recent volcanic eruption discovered on the central
432 Mariana back-arc spreading center. *Frontiers in Earth Science* **6**, 172 (2018).
- 433 65 Schipper, C. I., White, J. D., Houghton, B., Shimizu, N. & Stewart, R. B. Explosive
434 submarine eruptions driven by volatile-coupled degassing at Lōihi Seamount, Hawaii.
435 *Earth and Planetary Science Letters* **295**, 497-510 (2010).
- 436 66 Carey, R. *et al.* The largest deep-ocean silicic volcanic eruption of the past century.
437 *Science advances* **4**, e1701121 (2018).
- 438 67 Thordarson, T. & Self, S. The Laki (Skaftár Fires) and Grímsvötn eruptions in 1783-
439 1785 *Bull Volcanol* **55**, 233-263 (1993).
- 440 68 Neal, C. *et al.* The 2018 rift eruption and summit collapse of Kīlauea Volcano.
441 *Science* **363**, 367-374 (2019).
- 442 69 Cogné, J.-P. & Humler, E. Temporal variation of oceanic spreading and crustal
443 production rates during the last 180 My. *Earth and Planetary Science Letters* **227**,
444 427-439 (2004).

- 445 70 Marty, B. & Tolstikhin, I. N. CO2 fluxes from mid-ocean ridges, arcs and plumes.
446 *Chemical Geology* **145**, 233-248 (1998).
447 71 REVOSIMA, R. d. s. V. e. S. d. M. Bulletin n°16 de l'activité sismo-volcanique à
448 Mayotte, du 1 au 31 mars 2020. (2020).
449 72 Debeuf, D. *Étude de l'évolution volcano-structurale et magmatique de Mayotte,*
450 *Archipel des Comores, océan Indien: approches structurale, pétrographique,*
451 *géochimique et géochronologique*, (2009).
452 73 Stamps, D., Saria, E. & Kreemer, C. A Geodetic Strain Rate Model for the East
453 African Rift System. *Sci, Rep*, **8**, 732, doi:10.1038/s41598-017-19097-w (2018).
454 74 Deville, E. *et al.* Active fault system across the oceanic lithosphere of the
455 Mozambique Channel: implications for the Nubia–Somalia southern plate boundary.
456 *Earth and Planetary Science Letters* **502**, 210-220 (2018).
457 75 Macgregor, D. History of the development of the East African Rift System: A series of
458 interpreted maps through time. *Journal of African Earth Sciences* 101, 232-252
459 (2015).
460
461

462 Correspondence and requests for materials should be addressed to Nathalie Feuillet
463 (feuillet@ipgp.fr)

464

465

466 Author Information

467 Océane Foix

468

469 Present address : Montpellier 2 University, France

470

471 Manuel Moreira

472 Present address: Orleans University, France

473

474 Affiliations

475

476 Université de Paris, Institut de physique du globe de Paris, CNRS, F-75005 Paris, France

477

478 Nathalie Feuillet, Wayne C. Crawford, Christine Deplus, , Eric Jacques, Jean Marie Saurel,
479 Claudio Satriano, Océane Foix, Philippe Kowalski, Angèle Laurent, Manuel Moreira, Aline
480 Peltier, François Beauducel, Raphaël Grandin, , Romuald Daniel, Jérémy Gomez, Simon
481 Besançon, Pascal Bernard, Arnaud Lemarchand

482

483 IFREMER, Unité Géosciences Marines, Technopole La Pointe du Diable, 29280 Plouzané,
484 France

485

486 Stephan. Jorry, Chastity Aiken, Emmanuel Rinnert, Cécile Cathalot, Jean-Pierre Donval,
487 Vivien Guyader, Arnaud Gaillot, Carla Scalabrin, Pascal Pelleau, Louis Geli, Yves Fouquet,
488

489 Bureau de Recherches Géologiques et Minières - BRGM, DGR/GBS, F-45060 Orléans,
490 France
491 Isabelle Thinon, Anne Lemoine, Fabien Paquet, Didier Bertil
492

493 Littoral ENvironnement et Sociétés (LIENSs) UMR7266, Université de La Rochelle - CNRS,
494 2 rue Olympe de Gouges, 17000 La Rochelle
495
496 Valerie Ballu
497

498 Université Clermont Auvergne, CNRS, IRD, OPGC, Laboratoire Magmas et Volcans, F-
499 63000 Clermont-Ferrand, France,
500

501 Patrick Bachelery

502

503 Institut de Physique du Globe de Strasbourg UMR7516 CNRS Université de Strasbourg, 5
504 rue René Descartes 67000 Strasbourg, France
505

506 Jérôme Van der Woerd

507

508 **Acknowledgements**

509 We thank captain A. Eyssautier and the officers and the crew of the R/V *Marion Dufresne*
510 (TAAF/IFREMER/LDA), GENAVIR's coordinator, M. Boudou D'hautefeuille, and the
511 shipboard operations engineers. We thank the captain and crew of the M/V *Ylang* (SGTM
512 company). This research was supported by the French Ministries of Environment, Research
513 and Overseas under a research project to N.F. (proposal INSU-CT3 TELLUS SISMAYOTTE
514 2019). The french national geographic Institute (IGN) provided the Mayotte GNSS data. The
515 la Réunion university (Laboratory of atmosphere and hurricanes) provided data from the

516 DSUA station in Madagascar (contract INTERREG-5 Indian Ocean 2014-2020 "ReNovRisk-
517 Cyclones").

518 We thank CNRS/INSU, IPGP, IFREMER, BRGM for additional support under internal funds.

519 We thank our colleagues F. Tronel, A. Roulle, E. Dectot, A. Colombain, C. Doubre, Daniel
520 Sauter, Antony Dofal and Antoine Villié for assistance in the field, previous data acquisition,
521 processing and model development. We thank Olivier Desprez de Gesincourt, L. Testut and
522 T. Tranchant for loan and data processing of the seafloor pressure sensors. We thank the
523 French National Marine Hydrographic and Oceanographic Service (SHOM) for providing us
524 with previous data from the area. We thank G. Barruol for discussions. This is IPGP
525 contribution number XXXX.

526

527 **Author contributions**

528 NF, SJ, WCC, CD, IT, EJ, JMS, ALe, FP, RD, AG, CA, OF, PK, ALa, JPD, LG, JG, VG, PP,
529 ER participated on the MAYOBS1 cruise (NF, SJ and WCC as PI), acquired and processed
530 the geophysical and seismological data. CSa, ALa and PB detected and located the VLF
531 events. AP was in charge of the GNSS installation in Glorieuse island and processed and
532 modeled the GNSS data with FB and RG. VB was in charge of the OBSs APGs and
533 processed their data. SB participated in the first OBS deployment on the Ylang vessel with
534 WC and RD. DB, ALM and JWV were responsible for the installation of new seismological
535 and GNSS stations in Mayotte and of data acquisition onshore. JPD, VG, ER, CC performed
536 the geochemical analysis and interpretation of the water column data. CSc and AG processed
537 the EM122 acoustic data. CD and AG performed the depth changes calculation. CSc provided
538 the interpretation of the water column acoustic data. PBa and YF furnished the rocks sample
539 descriptions and petrological analysis. NF, SJ, CD, PBa, YF, IT, FP, JWV, EJ provided the
540 geological interpretation. NF wrote the paper with the contribution of all other authors. P.B.

541 JMS, EJ, WCC, CSa, PB, ALe, GL, CA, VB, AG, AP, FB, RG, ER, CC, CSc wrote the
542 method section and the supplementary material.

543

544 **Competing interests**

545 The authors declare no competing interests.

546 **FIGURE CAPTIONS**

547

548 **Figure 1: The volcanic ridge offshore Mayotte.** a) 3D Westward view of Mayotte island
549 and insular slope (vertical exaggeration 3). Green stars: Acoustically-detected plumes above
550 the Horseshoe, the NVE and the degassing area on Petite-Terre island. Left inset: geographic
551 setting and Global Navigation Satellite System (GNSS) surface horizontal displacements
552 stations. Black points: seismic stations. Dashed grey lines: Mesozoic fracture zones ⁶. b)
553 Geological interpretations of MAYOBS1 data. Purple patches: Volcanic structures (mainly
554 cones). Pink patches: lava flows and elongated features. Yellow patches: upper slope's high
555 reflective lava flows. NVE: in red (central part) and orange (radial ridges and flat flows).
556 Green stars as in a). Red lines: fissures and faults, dashed lines: inferred faults. black dots:
557 bathymetric depression. White boxes: location of Fig.2a and Extended data Fig. 3. Inset, as in
558 b with MAYOBS backscatter data. Pink dots: Ocean Bottom seismometer (OBS) seismicity:
559 yellow diamonds: location of the Very Low Frequency earthquakes. White boxes: location of
560 extended data Figure 3.

561

562

563 **Figure 2: The new volcanic edifice (NVE) offshore Mayotte.** a) 30 m resolution
564 bathymetric maps from shipboard EM122 multibeam, illuminated from N290°E. upper panel:
565 SHOM bathymetry collected in 2014 ¹⁹; lower panel: MAYOBS1 bathymetry collected in
566 May 2019 ¹⁸. black circle: position of dredge DR01. b) Depth changes between 2014 and
567 2019. The change in topography is estimated to be significant when larger than 10 m.

568

569

570 **Figure 3: The new volcanic edifice (NVE) and the acoustic plume.** a) Southward 3D view
571 of the NVE and the water column acoustic plume observed one hour before the Conductivity-

572 Temperature-Depth (CTD) rosette on May 16th 2019. The White dot and blue patch indicate
573 the position of the CTD rosette deployment, 1 km far from the summit the volcano. Right
574 inset: Processed polar echogram from one EM122 multibeam ping on May 16th (13:33 UT),
575 horizontal and vertical-axes (both in meters) correspond respectively to the cross-track
576 distance and the water depth.

577

578

579

580 **Figure 4: Conceptual model of the submarine eruption offshore Mayotte eruption.**

581 Bathymetry as in Figure 1b, no vertical exaggeration. Purple zones: N130°E volcano-tectonic
582 ridges and segments. Dashed white lines: inferred ancient caldera with degassing zones
583 above. Cross-section: red and reddish zones: magma storage zones (mush or magma
584 chambers) and magma pathways involved in the 2018-2020 Mayotte volcanic crisis and
585 seafloor eruption. Yellow layer: sediments. Dashed lines: subvertical faults beneath inferred
586 caldera possibly reactivated by the deflation of a deep reservoir. White arrow: possible
587 downsag at an initial stage of caldera collapse. Pink dots: 800 earthquakes located using
588 OBSs and land stations. Other dots: 139 earthquakes from before the OBS deployment:
589 colored dots are from the first 6 weeks of the crisis and white dots from the remaining 8
590 months before the OBS deployment. Yellow diamonds: Very Low Frequency (VLF)
591 earthquakes. Blue and red triangles: water and magma movements, respectively. Blue patch:
592 Location, with 3 sigma uncertainties, of the most robust isotropic source deformation model.
593 Moho depth from ³⁷. Lithosphere/asthenosphere boundary depth from ^{60,61}.

594

595

596 **Figure 5: Regional volcano-tectonic setting of the submarine eruption offshore Mayotte.**

597 a) Volcano-tectonic setting of the new volcanic edifice (NVE). Volcanic cones and ridges
598 (purple) from this study and ^{13,72,16,51}. Dots and diamonds : earthquakes as in Figure 4 and
599 Extended data Fig. 6 and 8. Focal mechanisms for M>5 earthquakes ⁴⁰. Dotted white arrow:
600 dyking intrusion along eastern segment of the Mayotte volcanic ridge. Red ellipse: inferred
601 main volcano-tectonic ridges. Purple ellipses: highly damaged zones in between the en
602 echelon ridges. Thick black arrows: local extension direction. Inset: sandbox model adapted
603 from ⁵⁸ illustrating the possible arrangement of the main volcano-tectonic structures in
604 Comoros. b) Geodynamic setting of the East African Rift systems. Main tectonic structures
605 and extensional zones in Africa and Madagascar from this study and ^{73,57,74,75,56}. Purple patches:

606 Quaternary volcanism in Madagascar ⁵⁷. Red dots: M> 2.5 earthquakes ⁴ with focal
607 mechanisms from ⁴⁰ for the M>5 earthquakes. Arrows: GNSS horizontal motions ⁷³. Small
608 purple ellipses in the Comoros as in a) with double dark red arrows: the volcanic ridge east of
609 Mayotte and extension direction. Inset: Simplified tectonic map of the East African Rift
610 system: Yellow highlights: most active rifts and graben; Red ellipse: Transfer zone of the
611 Comoros with direction of lateral motion.

612

613 **METHODS**

614 **Summary**

615 **Ship-borne Multibeam data** was acquired using a Kongsberg EM122 1°x1° during the 2014
616 ¹⁹ and 2019 ¹⁸. **Ship-borne Multibeam data** were processed with the GLOBE software ⁷⁶ to
617 provide 30-m grid spaced digital terrain models and seafloor backscatter imagery and to
618 calculate depth differences, surface and volumes. The 3D acoustic water column data from
619 the 2019 cruise were processed using SonarScope (@Ifremer) and GLOBE softwares
620 <https://doi.org/10.17882/70460> ⁷⁶. **Water column measurements:** A CTD-Rosette Seabird
621 911+ CTD (Conductivity; Temperature; Depth) equipped with an altimeter, an Aanderaa
622 oxygen optode and a Seapoint Turbidity Meter was mounted on a carousel with 16 ®Niskin
623 sampling bottles (8L) to measure and sample throughout the water column. Sub-sampling
624 was performed for onboard analyses (pH, alkalinity and total CO₂ by pH electrode and
625 titrator) and for onshore analyses (CH₄ analysis by the purge and trap method and H₂ and
626 CO₂ analysis by the Headspace method). **Seismology:** 800 earthquakes identified from the
627 onshore catalog were selected in descending magnitude order and manually picked onboard.
628 The seismic network used during the two month deployment included OBSs, onshore local
629 and regional stations (up to 500km distance). The events were relocated with NonLinLoc ⁷⁷
630 and an hybrid velocity model based on trials with 6 different velocity models, achieving final
631 location accuracies better than 5km. Eighty-four very low frequency (VLF) earthquakes were

632 detected between February 25 and April 24, 2019, using an amplitude trigger on ocean
633 bottom hydrophones recordings, filtered between 0.05 and 0.10 Hz, followed by a selection of
634 events with a clear peak frequency and a final visual inspection. VLF earthquakes were
635 located using spatial 3D back-projection of station-pair cross-correlation functions ⁷⁸,
636 assuming a constant surface-wave speed of 3.5 km/s. A well-constrained epicentral location
637 was obtained for 81 events. **Geodesy:** We inverted the surface deformation recorded by 6
638 permanent GNSS (Global Navigation Satellite System) receivers installed in Mayotte, Grande
639 Glorieuse and Madagascar. We used both an isotropic model and a triple volumetric
640 discontinuities (pCDM source) in a homogeneous elastic half-space, isotropic material with
641 Poisson's ratio of 0.25 to model the pressure source in depth. Seafloor pressure data (30s
642 sample interval) were pre-processed using harmonic analysis to remove the tides and low-pass
643 filtering to remove residual oscillations interpreted as internal waves.

644 **Water Column: Bathymetry and water column acoustic data.**

645 *See also Extended Data Figures 1 to 3 and Figure 5*

646 We mapped the submarine slope and basin adjacent to Mayotte and detected and mapped
647 water column anomalies using ship-borne multibeam surveys over an area of 8600 km².
648 Bathymetric data were collected in 2014 by the French *Service Hydrographique et*
649 *Océanographique de la Marine* ¹⁹ using the vessel BHO Beautemps Beaupré. The 2019 data ¹⁸
650 were collected using the R/V Marion Dufresne during the MAYOBS1 cruise (May 3rd to
651 18th). Both vessels are equipped with identical Kongsberg EM122 multibeam echosounders
652 (12 kHz, 1°x1° beam width). Bathymetry and seafloor backscatter data sets were processed
653 using the GLOBE software ⁷⁶ with identical 30-m cell grids to allow accurate estimates of
654 differences in depth, surfaces and volumes. Water column acoustic data are only available for
655 the 2019 cruise and processing was performed onboard using the SonarScope (@Ifremer) and
656 GLOBE software packages using published methods ⁷⁹.

657

658 **Water column: Sampling and chemical analysis**

659 *See also Extended Data Figure 4.*

660

661 ***Water column sampling and in situ measurements with CTD-Rosette.***

662 Seawater was sampled using IFREMER's CTD-Rosette, consisting of a Seabird 911+ CTD
663 (Conductivity; Temperature; Depth) instrument mounted on a carousel with 16 8-liter[®] Niskin
664 sampling bottles. For this cruise, the CTD-Rosette was equipped with an altimeter, an
665 Aanderaa oxygen optode and a Seapoint turbidity meter. Information from the sensors was
666 transmitted in real time, allowing us to adapt the sampling strategy to observed water column
667 anomalies.

668 The[®] Niskin bottles were subsampled for onboard and onshore analyses. For CH₄ analysis,
669 125mL glass bulbs were used for analysis using the purge and trap method. The bulbs were
670 allowed to overflow by at least two volumes of seawater and particular care was taken to
671 exclude air bubbles to prevent contamination. While filling, sodium azide was added to
672 prevent future microbial activity. For H₂ and CO₂ analysis, 160 mL vials were filled using the
673 Headspace method. The vials, containing some sodium azide, were filled using a silicone tube
674 connected to the[®] Niskin bottle. The silicone tube was inserted to the bottom of the vial in
675 order to completely fill the vial from the bottom to the top, displacing all contained air. The
676 tube was then slowly removed, taking care to avoid any air bubble, and the vial was sealed
677 with a PTFE septum using special crimping pliers. The headspace volume of 10 mL of
678 atmospheric air was added using a needle mounted on a syringe.

679

680 ***CH₄ analysis by the purge and trap method at IFREMER laboratories.***

681 Onshore, the Purge and trap method⁸⁰ was used. Once in the laboratory, CH₄ was stripped
682 from seawater using Helium carrier gas, trapped on activated charcoal at -80°C and detected

683 and quantified with a flame ionization detector after separation on a packed column.
684 Calibration was performed injecting of a commercial gas standard (CH₄ 107.8ppm). The limit
685 of detection is 0.03nmol/L, the precision (based on five replicates from the same rosette
686 bottle) is within ± 2% (confidence level 95%) and the accuracy is 5%. The CH₄ equipment
687 was set up in a portable clean air-conditioned container, allowing one CH₄ analysis every 6
688 min using two extraction kits.

689 **CO₂ and H₂ analysis** were performed at IFREMER laboratories by GC/HID following
690 methods described in ⁸¹, except that the headspace vial replaced the syringe.

691

692 **pH, Total Alkalinity and ΣCO₂ measurements onboard.**

693 pH, Total Alkalinity and ΣCO₂ measurements were performed onboard using a Metrohm 848
694 Titrino Plus titrator. The pH electrode was calibrated using commercially available pH
695 buffers. pH was measured as soon as possible after sample recovery and Total Alkalinity and
696 ΣCO₂ were then determined by direct titration with 0.1N hydrochloric acid. Concentrations
697 were compared to a seawater reference for oceanic CO₂ measurements (Batch 178).

698

699

700 **Seismology data**

701 *See also Supplementary information and Extended Data Figures 6 and 8*

702 The 800 earthquakes discussed in this paper were located using recordings from a network of
703 up to 22 seismological stations equipped with sensors of different types, operating during
704 different time slots comprised between February 25th and May 5th 2019: 6 ocean bottom
705 seismometers (OBS) and up to 16 land stations on Mayotte island, on Grande Glorieuse, on
706 Khartala volcano, in Madagascar and in Kenya. Details on station location, type and quality
707 are provided in Supplementary Information Figures S2.1 and S2.2 and Table S2.1.

708 An earthquake catalog of 2362 events of magnitude $2.0 < M < 5.4$, between February 25th and
709 May 5th, was produced in near real-time by BRGM using land stations⁸². On board, three
710 groups of operators working around the clock manually picked 800 of the events from the
711 OBS, selected in descending magnitude order, using SeisComP3 software⁸³. The Hypo71
712 software⁸⁴ was used for preliminary locations and SeisComP3 was used to compute ML and
713 MLv magnitudes, the velocity model was updated to fit the data (see Supplementary S2) then
714 the NonLinLoc (NLL) software⁷⁷ was used to relocate the events. Low-frequency events
715 were detected and analysed using the broadband land stations and the broadband hydrophone
716 (HiTech HTI-90U, 30s cut-off frequency) on the OBSs.

717

718 **Geodesy data**

719 See Supplementary Material and Extended Data Figures 7

720 We used the GNSS stations from the Centre National d'Etudes Spatiales (MAYG),
721 EXAGONE's TERIA network (BDRL and GAMO), Precision Topo's Lel@ network
722 (KAWE), IGP (GLOR) and the Université de la Réunion (DSUA). Sea floor pressure data
723 were collected using Seabird SBE37 pressure sensors deployed on the OBS frames. The
724 seawater pump of each instrument was deactivated to avoid induced noise on the seismometer
725 recordings. Although SBE37s are not designed for seafloor geodesy, previous experiments
726 indicate that their pressure gauge can be used to characterize sudden or large-amplitude
727 deformations^{85,86}.

728

729

730

731 **Data availability statement**

732 The authors declare that most of the data supporting the findings of this study are available
733 within the paper and its supplementary information files. GNSS data are available on the
734 website « <http://mayotte.gnss.fr> » and can be downloaded on this ftp site
735 ftp://rgpdata.ign.fr/pub/gnss_mayotte/. Ship-borne geophysical data from the MAYOBS1
736 cruise can be obtained through the French national oceanographic data center SISMER
737 (<http://en.data.ifremer.fr/SISMER>) but restrictions apply to the availability of these data. The
738 compilations of older bathymetric and topographic data are available on the SHOM Website
739 (<http://www.shom.fr>). Rock samples are referenced at
740 <https://wwz.ifremer.fr/echantillons/Echantillons/Carte#/map>
741 and <https://campagnes.flotteoceanographique.fr/search>. Samples are accessible on site at
742 IFREMER, Plouzané, France.

743 Map were created using Globe software <https://doi.org/10.17882/70460>⁷⁶, ArcGIS® software
744 by Esri (<https://www.arcgis.com/index.html>), Generic Mapping Tools⁸⁷, Adobe illustrator®
745 (<https://www.adobe.com/>) and MATLAB.

746 In addition to Mayobs 1 cruise multibeam data (resolution: 30m)¹⁸, Figs. 1, 2, 4, 5 and
747 Extended data Fig. 1, 2, 3, 6, 7, 8, 9 include topographic and bathymetric data from previous
748 compilation^{16,88,89,90}, the General Bathymetric Chart of the Oceans (<https://www.gebco.net>)
749 and Global topography from SRTM GL1 ([https://catalog.data.gov/dataset/shuttle-radar-](https://catalog.data.gov/dataset/shuttle-radar-topography-mission-srtm-gl1-global-30m)
750 [topography-mission-srtm-gl1-global-30m](https://catalog.data.gov/dataset/shuttle-radar-topography-mission-srtm-gl1-global-30m)). Litto3D Mayotte
751 (<https://diffusion.shom.fr/presentation/litto3d-mayot2012.html>). Topography and bathymetry
752 of Figure 5b from GeoMapApp (www.geomapapp.org) / CC BY. In Fig 5 and Extended data
753 Figs.6, 8, 9: focal mechanisms for M>5 earthquakes are from⁴⁰. In Figure 5, M> 2.5
754 earthquakes are from⁴

755

756 **Code Availability**

757 **Ship-borne Multibeam data** were processed with the GLOBE software ⁷⁶. The 3D acoustic
758 water column data were processed using SonarScope (@Ifremer) and GLOBE softwares
759 <https://doi.org/10.17882/70460> ⁷⁶. GNSS solutions were computed using the GipsyX/JPL software
760 available at <https://gipsy-oasis.jpl.nasa.gov>. Deformation source modeling codes (Mogi and
761 Nakkhoo) are available at <https://github.com/IPGP/deformations-matlab> and data processing
762 has been achieved using the WebObs open-source system available
763 at <https://ipgp.github.io/webobs/>.

764 Pressure gauge data were processed with Python ⁹¹. Very Low Frequency Event analysis has
765 been performed using ObsPy ⁸⁹ NumPy ⁹² and Matplotlib ⁹³. Earthquake phase picking was
766 performed with SeisComP3 ⁹⁴ and initial locations used Hypo71 ⁸⁴
767 Final locations were performed with NonLinLoc ⁷⁷ and
768 results converted back to SeisComP3 using ObsPy ⁸⁹.

769

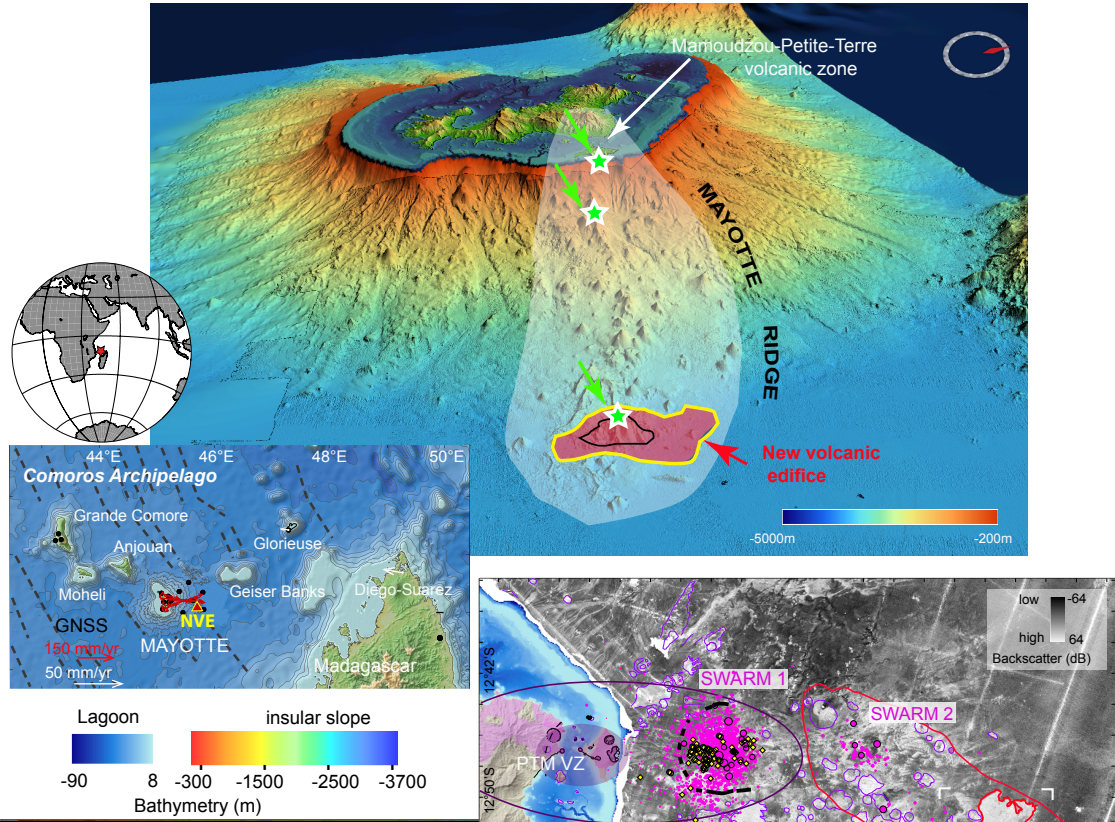
770
771
772
773
774

Method References

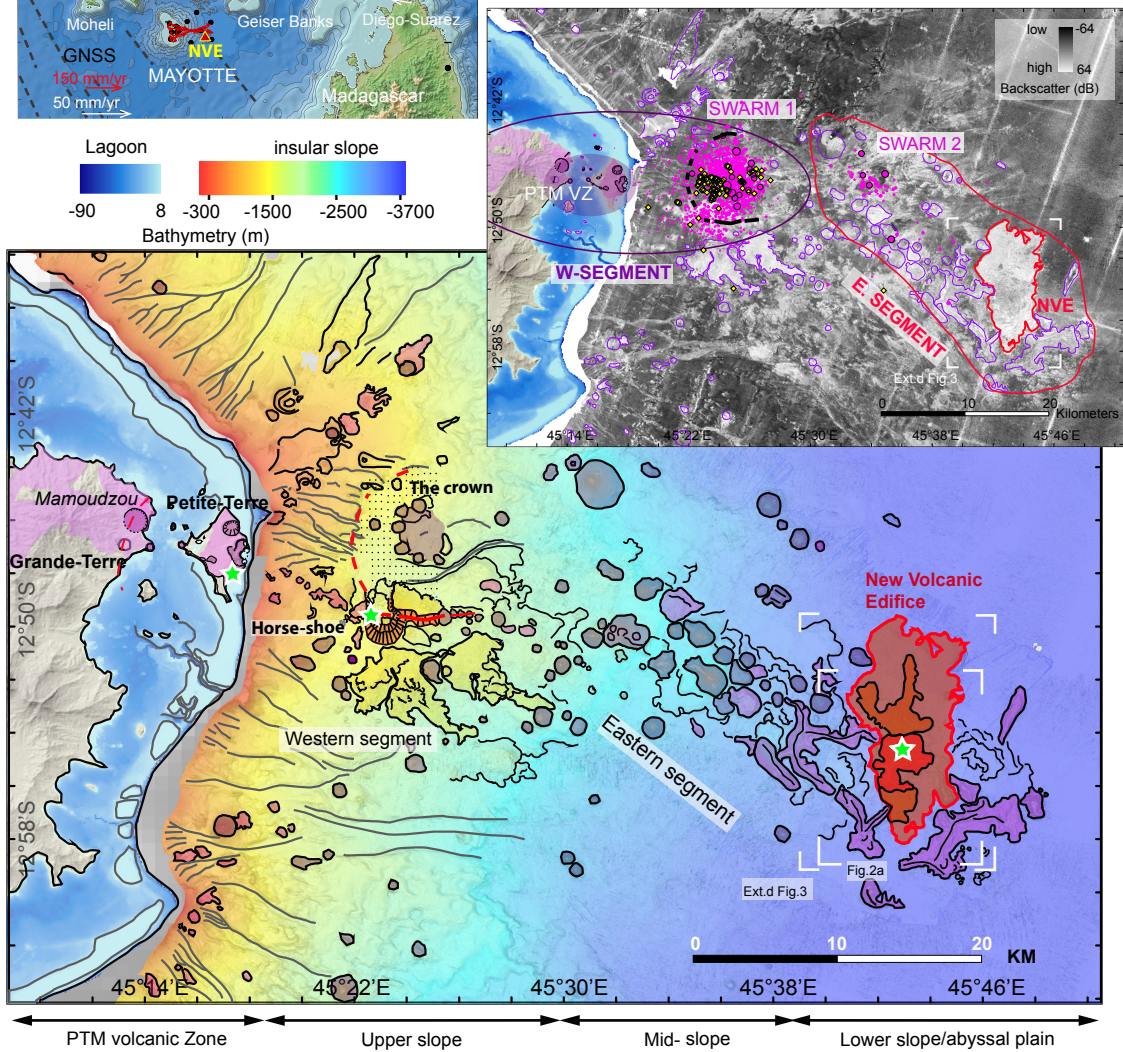
775
776

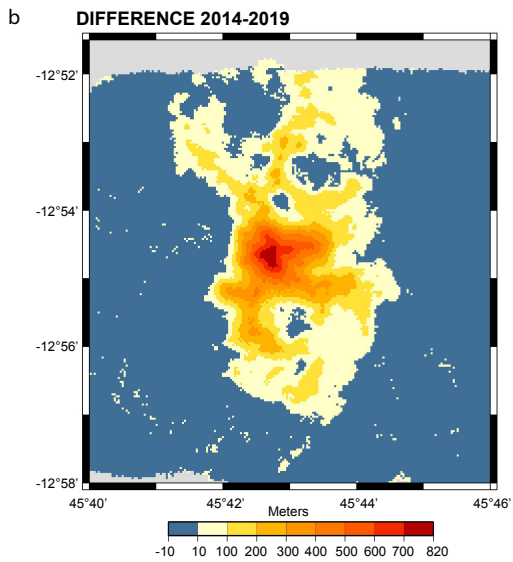
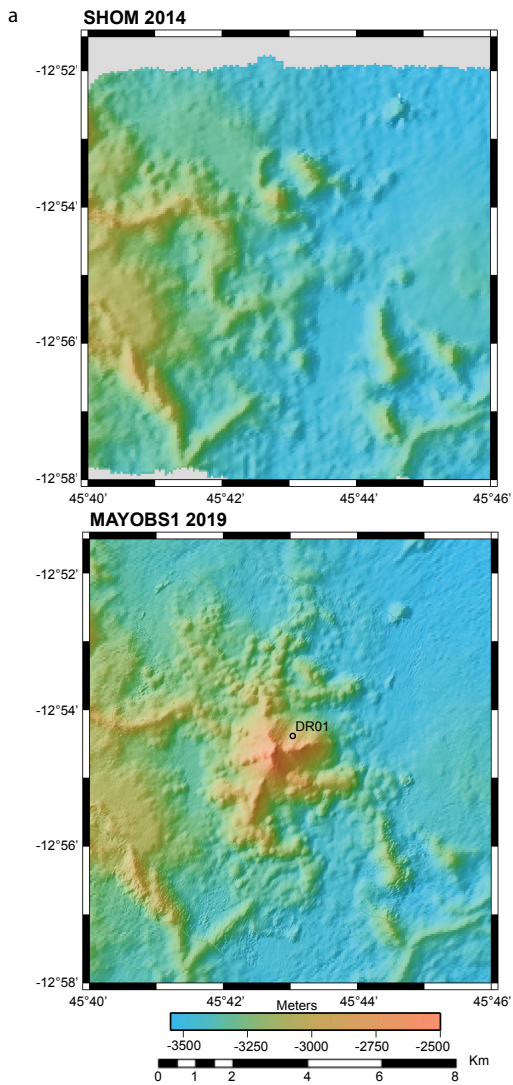
- 777 76 Globe (GLObal Oceanographic Bathymetry Explorer) Software. (2020).
778 77 Lomax, A., Michelini, A. & Curtis, A. Earthquake location, direct, global-search
779 methods. *Encyclopedia of complexity and system science* **5**, 1-33 (2009).
780 78 Poiata, N., Satriano, C., Vilotte, J.-P., Bernard, P. & Obara, K. Multiband array
781 detection and location of seismic sources recorded by dense seismic networks.
782 *Geophysical Journal International* **205**, 1548-1573 (2016).
783 79 Dupré, S. *et al.* Tectonic and sedimentary controls on widespread gas emissions in the
784 Sea of Marmara: Results from systematic, shipborne multibeam echo sounder water
785 column imaging. *Journal of Geophysical Research: Solid Earth* **120**, 2891-2912
786 (2015).
787 80 Charlou, J. L., Dmitriev, L., Bougault, H. & Needham, H. D. Hydrothermal CH₄
788 between 12 N and 15 N over the Mid-Atlantic Ridge. *Deep Sea Research Part A.*
789 *Oceanographic Research Papers* **35**, 121-131 (1988).
790 81 Donval, J.-P. & Guyader, V. Analysis of hydrogen and methane in seawater by
791 “Headspace” method: Determination at trace level with an automatic headspace
792 sampler. *Talanta* **162**, 408-414 (2017).
793 82 Bertil.D, Lemoine.A, Colombain.A, Maisonhaute.E & Dectot.G. (BRGM, Orléans,
794 France, 2018).
795 83 Hanka, W. *et al.* Real-time earthquake monitoring for tsunami warning in the Indian
796 Ocean and beyond. *Natural Hazards & Earth System Sciences* **10** (2010).
797 84 Lee, W. H. K. & Lahr, J. C. *HYPO71: A computer program for determining*
798 *hypocenter, magnitude, and first motion pattern of local earthquakes.* (US
799 Department of the Interior, Geological Survey, National Center for ..., 1972).
800 85 Vilaseca, G. *et al.* Oceanographic Signatures and Pressure Monitoring of Seafloor
801 Vertical Deformation in Near-coastal, Shallow Water Areas: A Case Study from
802 Santorini Caldera. *Marine Geodesy* **39**, 401-421 (2016).
803 86 Fox, C. G. In situ ground deformation measurements from the summit of Axial
804 Volcano during the 1998 volcanic episode. *Geophysical Research Letters* **26**, 3437-
805 3440 (1999).
806 87 Wessel, P. & Smith, W. H. New, improved version of Generic Mapping Tools
807 released. *Eos, Transactions American Geophysical Union* **79**, 579-579 (1998).
808 88 SHOM. (MNT_MAY100m_HOMONIM_WGS84, 2016).
809 89 Krischer, L. *et al.* ObsPy: A bridge for seismology into the scientific Python
810 ecosystem. *Computational Science & Discovery* **8**, 014003 (2015).
811 90 JORRY, S. (2014).
812 91 Van Rossum, G. & Drake, F. L. *Python reference manual.* (iUniverse Indiana, 2000).
813 92 Harris, C. R. *et al.* Array programming with NumPy. *Nature* **585**, 357-362 (2020).
814 93 Hunter, J. D. Matplotlib: A 2D graphics environment. *IEEE Annals of the History of*
815 *Computing* **9**, 90-95 (2007).
816 94 Weber, B. *et al.* in *Geophysical Research Abstracts.*
817

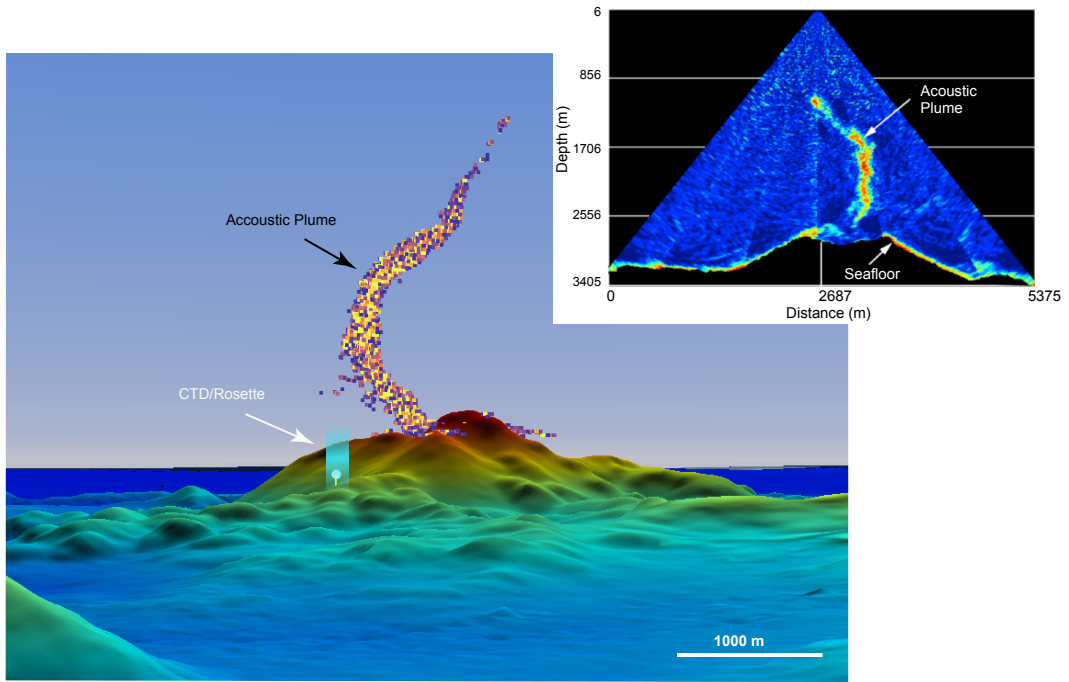
a

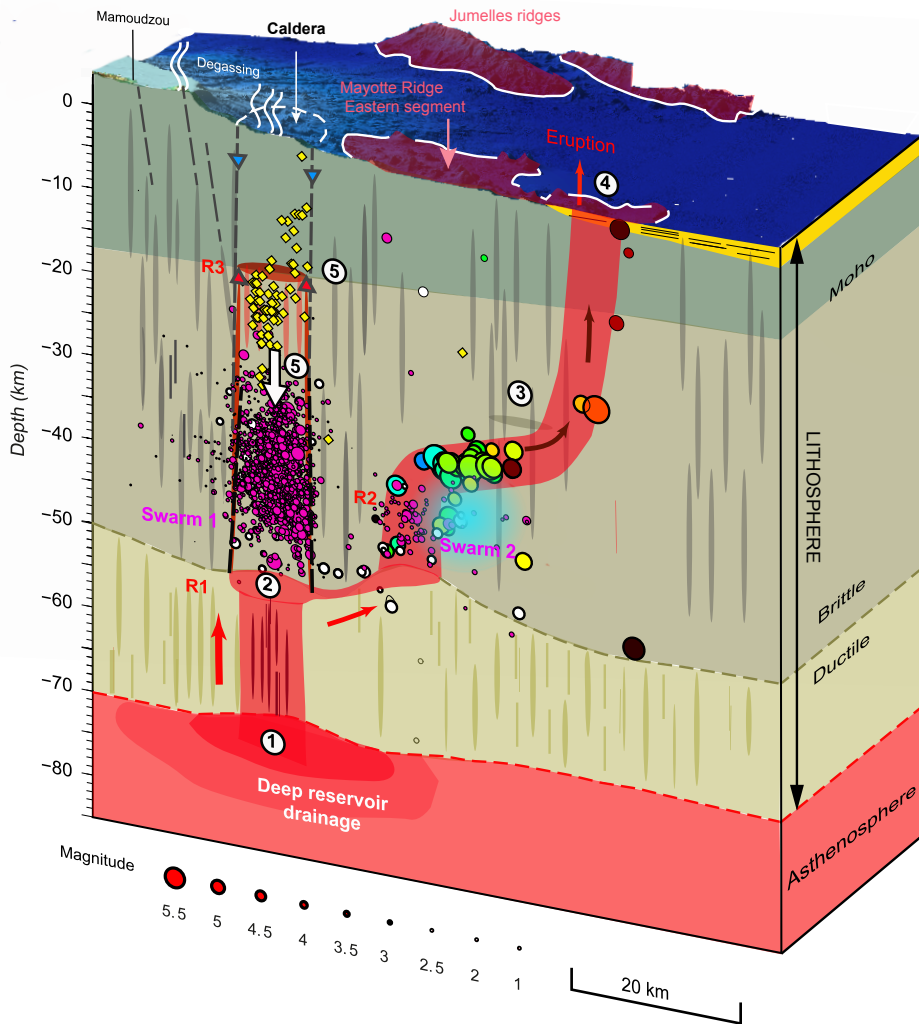


b









Chronology

- ① Deep asthenospheric reservoir drainage (before May 10 2018)
- ② slow refilling of the deep reservoir (before May 10 2018)
- ③ Reservoir failure/Dyking (May-June 2018)
- ④ Start of the eruption (July 2018) lithospheric reservoirs drainage
- ⑤ Reactivation of faults beneath ancient caldera ? (Sept 2018) + Fluid movement (magma/water)?

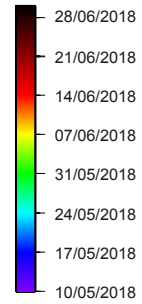
Seismicity time scale

MAYOBS1 data
(26/02/19 - 6/05/2019)

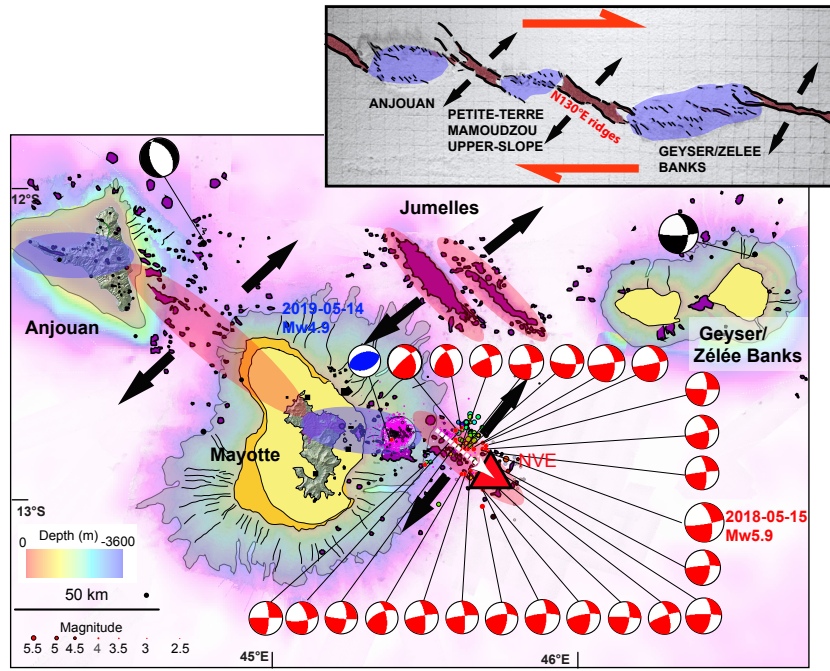
● VT ◆ VLF

Before OBS deployment

○ 07/18-02/19



a



b

